Isotacticity in chiral phononic crystals for low-frequency bandgap

Wei Ding, Tianning Chen, Dewen Yu, Chen Chen, Rui Zhang, Jian Zhu, Badreddine Assouar

Isotacticity in chiral phononic crystals for low-frequency bandgap

Wei Ding[a], Tianning Chen[a], Dewen Yu[b, c], Chen Chen[a], Rui Zhang[a], Jian Zhu[a, *], Badreddine Assouar[d, *]

[a]School of Mechanical Engineering, Xi'an Jiaotong University, Xi'an, Shaanxi 710049, PR China

[b]Key Laboratory of Ministry of Education for Modern Design and Rotor-Bearing System, School of Mechanical Engineering, Xi'an Jiaotong University, Xianning West Road, Xi'an 710049, China

[c]School of Civil and Environmental Engineering, Nanyang Technological University, 50 Nanyang Avenue, 639798 Singapore, Singapore.

[d]Université de Lorraine, CNRS, Institut Jean Lamour, F-54000 Nancy, France

[*]Corresponding authors. E-mail addresses: jianzhuxj@xjtu.edu.cn (J. Zhu), badreddine.assouar@univ-lorraine.fr (B. Assouar).

Abstract

Realizing a low-frequency and broad bandgap is extremely challenging because the lattice constant, equivalent stiffness, and equivalent density must be taken into account in practice. Despite the advances of inertial amplification which is one of the ideal strategies to address this issue, the design ideas are mainly limited to the classic geometries featured by mirror symmetry (syndiotacticity), confining then progress in this topic. Here, we report numerical and experimental investigation of a chiral phononic crystal without mirror symmetry (isotacticity) according to the analogous Thomson scattering. Numerical analysis shows that due to the lack of one degree of freedom in isotactic lattice (ISL) compared to syndiotactic lattice (SYL), the bandgap starting-frequency of the ISL is significantly lower than that the one of the SYL by up to 66%. The bandgap properties are further demonstrated by simulation and experimental measurements. This research reveals that the condition of having alternating arrangement orientations between neighboring atoms is not indispensable for this kind of

bandgap, and a rational geometry satisfying the Thomson scattering-based bandgap conditions can further reduce the bandgap frequency without affecting the stiffness and lightweight of the structure.

1. Introduction

The bandgap in phononic crystals provides a new path to high device performance in vibration isolation [1, 2], thermal insulation [3, 4], and robust topological wave transmission [5, 6]. In terms of the low-frequency and broadband isolation for elastic waves, the great efforts inspired by Bragg scattering [7] and local resonance [8] have been done, such as rainbow trapping [9-11], gradient distribution [11-15], coupled Bragg scattering and local resonance [16-19], acoustic black holes [20, 21], or nonlinear local resonance [22-25]. Even, the quasi zero stiffness, another one of appealing strategies, might be a solution of this dilemma because it can lower the frequency of the Bragg scattering bandgap [26-28], nevertheless the robustness and stability of the system is debatable when the metastructures are at the quasi-zero state. In general, these strategies are based on sacrificing the stiffness or (and) the lightweight of the system. It is indisputable that absolute ultra-low and ultra-wide bandgaps can be achieved as long as discounting the static properties such as lattice constants, equivalent stiffness, and static equivalent density [29-34]. However, these static properties are critical to ensure superior stability, reliability, and maneuverability of the high-performance devices in engineering practice. Therefore, overcoming the conflict between low-frequency and broad bandgaps and those three properties still remains great challenges.

In 2007, Yilmaz et al. proposed the inertial amplification to solve the above challenge [35]. In the inertial amplification system, the static inertia can be amplified many times, as a result, it can break the dependency of the local resonance and Bragg scattering on the stiffness and mass [35, 36]. The anti-resonance frequency in this structure can enhance the attenuation in low frequency [37-39]. Inspired by the inertial amplification, more and more novel studies are proposed. For instance, an octahedron structure was built to isolate the special omnidirectional elastic waves [40]; incorporating inertial amplification structures in continuous beams to manipulate the transverse wave [41, 42]; a 2D thin plates embedded the classical inertial amplifier structures was proposed to modulate low-frequency and broad lamb waves [43, 44]; the low-frequency vibration isolation of the corrugated-core

sandwich panels can be enhanced through embedding the inertial amplification system [45]; a lever-type inertial amplification system can achieve the broadband isolation for the surface wave which is induced by the seismic [46, 47]; the combination of the inertial amplification and local resonance can improve the extremely narrow effective attenuation of the classical local resonance bandgap [48] and release the dependence on lowering stiffness and increasing mass for low-frequency local resonance bandgap [49]; the multiple, broadband and highly attenuative bandgaps can be obtained by a system with inertial amplification, local resonance, and Bragg scattering affect simultaneously [50]. However, in the last two decades, the design strategies [42, 45, 51-55] have been limited to the form of the classical inertial amplification sub-structure.

In recent years, the inertial amplification was demonstrated in the axis twist metamaterials as well [56, 57]. Subsequently, an analogue of Thomson scattering was proposed theoretically, numerically, and experimentally to describe its underlying physics [58]. From the physics point of view, the coupling of orthogonal polarizations is a means to amplify the inertia [56, 57, 59], while the destructive interference is another key factor in opening the bandgap [58]. Achieving destructive interference relies on secondary scattered waves of the same polarization having opposite motion directions [58]. Based on this, a planar orthorhombic chiral lattice based on Thomson scattering was reported recently [60], in which an ultra-broad bandgap was achieved. It's worth noting that, an identical geometric feature can be observed from these studies [35, 57, 61-63], i.e., these geometries have a distinctive feature of alternating movement orientations between adjacent atoms (described as syndiotacticity [57] for convenience).

In fact, according to the three conditions for the bandgap generation [58], it is possible to achieve this bandgap even if the adjacent atoms in this non-mirror chiral lattice do not have alternating arrangement directions (isotacticity) as long as the horizontal tangential motion of the planar non-mirror chiral lattice (three-triplet lattice) is suppressed. Since the ligaments between adjacent lumped masses are continuous, theoretically, the number of wave reflections can be effectively reduced, which in turn reduces the resonance peaks in the FRF. Eventually, a bandgap with lower frequency than the mirror lattice will be produced.

Here, a planar chiral phononic crystal with non-mirror feature is proposed. To differentiate from the classic models, we name the phononic crystals with mirroring property which have Thomson scattering-induced bandgaps as syndiotacticity, and the other one with non-mirror property as isotacticity. To emphasis the novelty in this work, an isotactic lattice (ISL) and a syndiotactic lattice (SYL) are compared on the condition of the same lattice constant, equivalent stiffness, and density. We demonstrate that although both ISL and SYL satisfy the Thomson scattering conditions, i.e., orthogonal motions coupled to the lumped masses and the opposite motion directions in the second scattering, and because of the lack of the symmetry, at the starting boundary of the attenuation, ISL has one less resonant peak than SYL, thus, inducing a lower-frequency bandgap than that of SYL.

2. Structures and results

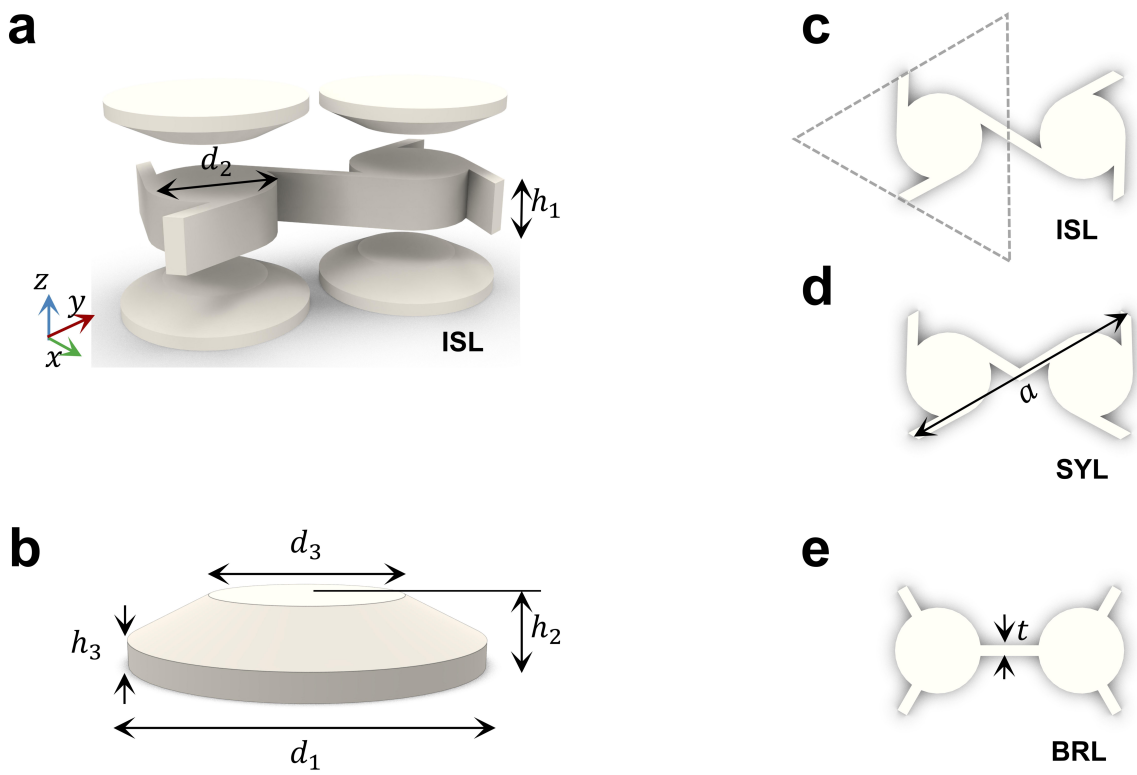

Fig. 1. (a) Schematics of the arrayed lattice (ISL). (b) Dimensions of the lumped mass. (c)-(e) The various in ligaments between ISL, SYL, and BRL.

Tacticity is a concept in polymer science to describe the relative orientation of adjacent chiral centers [64, 65]. This concept was firstly introduced in the chiral phononic crystal to describe the bandgap variances in syndiotactic lattice (SYL) and isotacticic lattice [57]. To facilitate the distinction, we state

syndiotacticity and isotacticicity to define the lattice with mirror and non-mirror features, respectively. To clarify the novelty of this study, SYL, ISL and Bragg scattering lattice (BRL) are discussed together. **Fig. 1**(a) shows the ISL schematic with lattice constant a=80 mm, d_1=37 mm, d_2=30 mm, d_3=27 mm, h_1=10, h_2=8 mm, h_3=3 mm, and t=2.5 mm. The details of the lumped mass can refer to **Fig. 1**(b). It should be stated that the shape of the lumped mass is intended to obtain the inertia amplification factor as larger as possible [66]. Meanwhile, it should be note that three sorts of lattice have the same outline except the shape of the ligaments. As illustrated in **Fig. 1**(c)-1(e), the ligament in ISL is tangent with the circle whose diameter is d_2. SYL is by mirroring the sub unit cell of ISL (highlighted by gray dotted line in **Fig. 1**(c)). In BRL, the centerline of the ligament is perpendicular to the tangent of the circle with d_2.

Traditional phononic crystals consisted of a homogeneous continuous matrix and periodic scatterers, so the non-dimensional bandgap was evaluated using normalized criteria of the material acoustic speed and lattice constants [17, 67]. Later, the quadratic tailoring matrix was proposed because it can drastically enhance the impedance between the matrix and scatterers, thus realizing an absolute low-frequency and broadband Bragg scattering bandgaps [29, 68]. Observing from kinetic equation, the enhancement of the impedance reduces the equivalent stiffness or (and) equivalent density of the system, i.e., these two metrics (equivalent stiffness and equivalent density) are inversely proportional to the bandgap starting frequency [66, 69, 70]. Therefore, the bandgap evaluation should take into account the equivalent stiffness and equivalent density in addition to the lattice constant. In order to fairly evaluate these three bandgaps, we use Eq. (1) to normalize the band structure.

$$f_n = fa\sqrt{\frac{m_e}{k_e}}, \tag{1}$$

where $m_e = 0.15$ kg in three lattices. To obtain the equivalent stiffness, using ANSYS workbench LS-dyna simulates the compression for the geometric models shown in **Fig. 2**(a-c). The material is one kind of Nylon with the elastic modulus $E = 1.6 \times 10^9$ Pa, Poisson's ratio $v = 0.4$, and density $\rho = 1000\ \mathrm{kg/m^3}$. h_1 equals 20 mm to avoid the z-axis deformation. We should note that the thickness h_1 of the models shown in **Fig. 2**(a-c) is two times of that in bandgap calculation, therefore, the actual stiffness of the models in the normalized bandgap is 0.5 times of the stiffness denoted in **Fig. 2**(e). However, in the normalized band structure, because the stiffness of BRG, ISL, and SYL is missing a

same coefficient which is 0.5 times, there is no influence on the fair comparison. Plate a is fixed and plate b has a velocity of 500 mm/s along the $-x$ axis. For convergence, the contact frictional coefficient between the sample and plates a and b, and between the sample and itself is 0.1 [71]. As shown in **Fig. 2**(d), the strain of the system focuses on the ligaments, that means the equivalent stiffness is mainly determined by the ligaments. This is the reason that we neglect the contribution of the lumped mass to the equivalent stiffness in order to speed up the calculation.

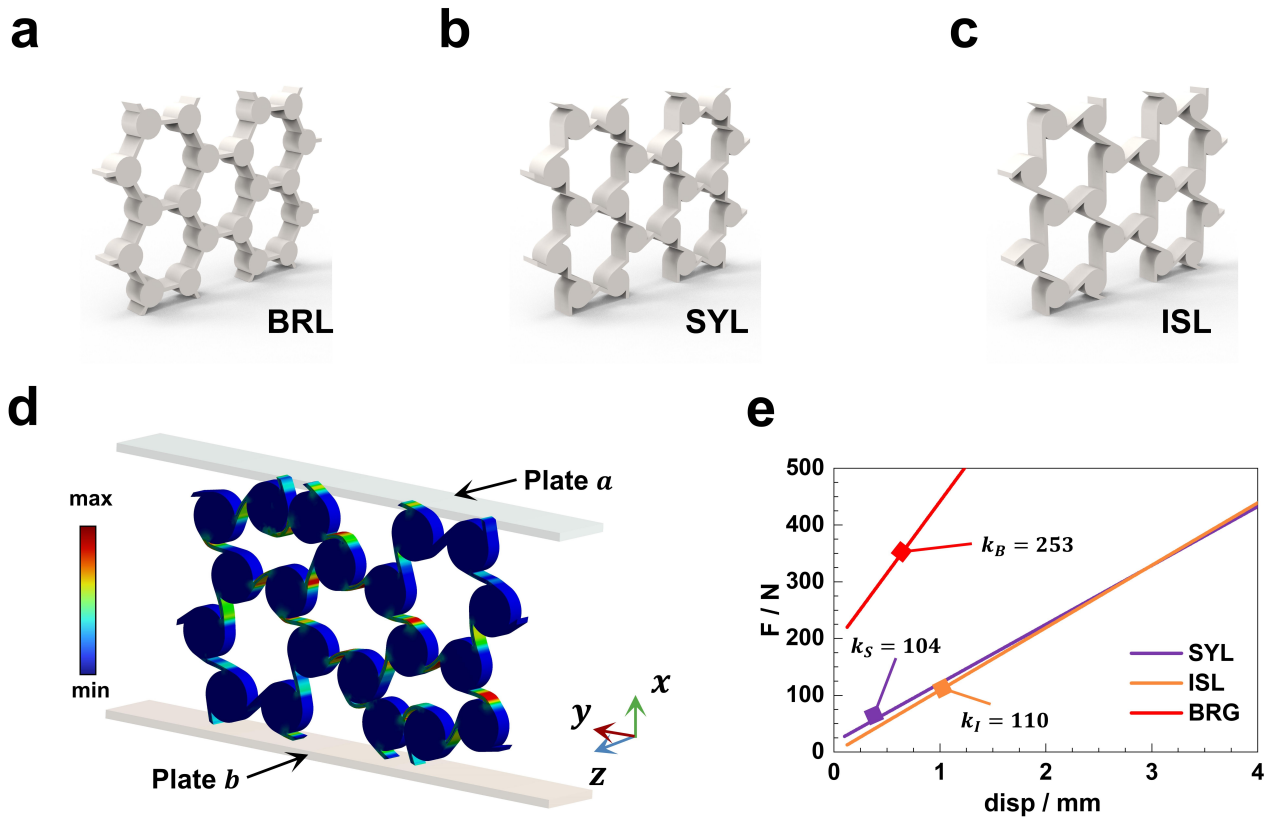

Fig. 2. (a) – (c) structure schematics of ISL, SYL, and BRL in compression simulation, respectively. (d) Equivalent stress contour of ISL when the displacement is 4 mm. (e) Fitted force-displacement results of ISL, SYL, and BRL, where k_B, k_S, and k_I means the stiffness of BRG, SYL, and ISL, respectively.

Fig. 2(e) shows the force-displacement results in linear elastic stage. Remarkably, although ISL and SYL have distinct configurations in ligaments, ISL (k_I=110 N/mm) and SYL (k_S=104 N/mm) have almost identical equivalent stiffness, which effect has been verified experimentally in our previous study [60]. Because of the distinct ligament configuration of the BRL, its equivalent stiffness is k_B=253 N/mm and significantly higher than the other two results. Because the stiffness is a key factor

effecting on the frequency, as a result, it requires us to normalize the band structures (**Fig. 3**) using Eq. (1) for a fair appraisal.

Fig. 3 shows the band structures calculated in COMSOL Multiphysics. In simulation, Bloch period boundary is applied in the unit cell and the band structures can be obtained through sweeping along the wave vector Γ-X-M-Γ as shown in **Fig. 3**(a). Due to the fact that translation and rotation are coupled only in the xoy plane; the degree of freedom of the ligaments along the z-axis are constrained to avoid the interference from out-of-plane modes.

The band structures in non-dimensional range of 0.5 are presented **Fig. 3**(a-c). In classic BRL (**Fig. 3**(a)), a broad bandgap extending from 0.0949 to 0.318 can be found. However, the bandgap of SYL (**Fig. 3**(b)), extending from 0.074 to 0.488, is broader than BRL. The most prominent is that ISL (**Fig. 3**(c)) has two bandgaps. The first one extends from 0.0251 to 0.117 and the other one from 0.193 to 0.488. When the bandgap width is evaluated at the center frequency of the bandgap [72], their relative widths are 1.08 (BRL), 1.47 (SYL), and 1.29 & 0.866 (ISL), respectively.

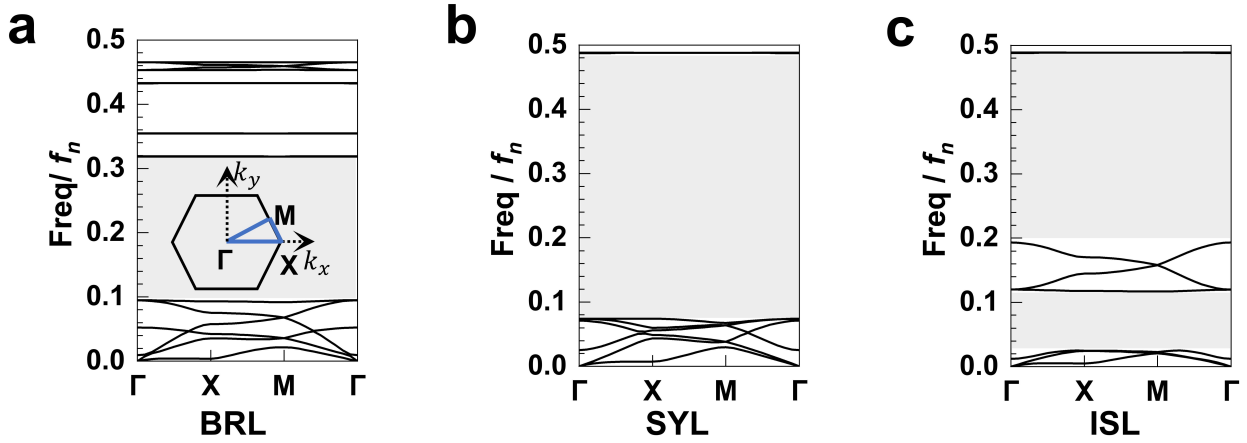

Fig. 3. Normalized band structures of BRL, SYL, and ISL. The shaded areas indicate the bandgaps.

Comparing with BRL, one can see that ISL and SYL have significant advantages in width and bandgap starting frequency of the first bandgap. It cannot be denied that SYL has a wider first bandgap than ISL. Nevertheless, the bandgap frequency of ISL is 66% lower than that of SYL, which occurs at the same lattice constant, same static equivalent density and quasi-identical equivalent stiffness. This is an encouraging result as it practically verifies the arguement [57] that the combination of inertial amplification and alternating arrangement orientations of adjacent atoms is merely one special case

for this bandgap formation. This indirectly demonstrates that the analogous Thomson scattering [58] has universality.

3. Bandgap mechanism

To illustrate the bandgap mechanism of ISL and the cause of the bandgap difference between ISL and SYL, we simplify ISL and SYL with 2D periodicity to a one-dimensional model and simulate the transmission of an ISL and an SYL. The models are presented in **Fig. 4**(a) and **Fig. 4**(d).

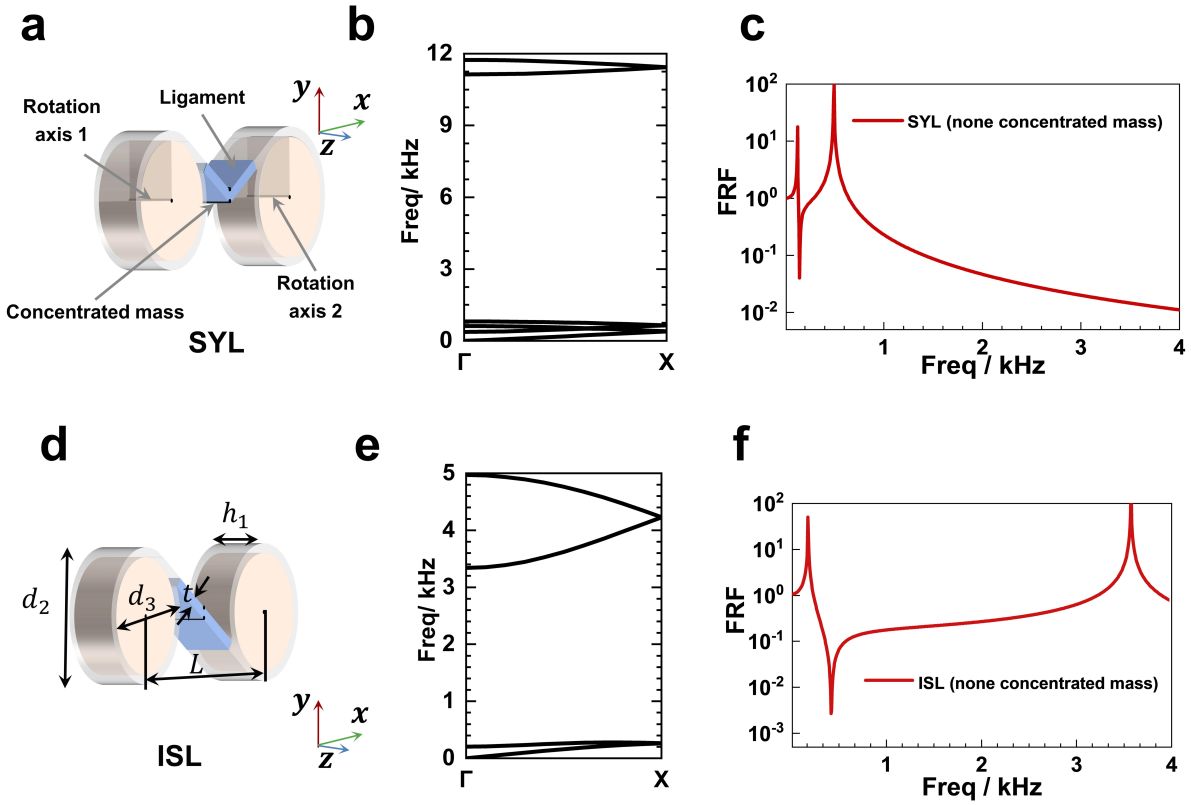

Fig. 4. (a) Simplified ISL unit cell. Blue domain indicates the ligament and the remaining part is lumped masses. Two black lines in the ligament denote the location of the concentrated mass m_a, and the concentrated mass is not considered the shape in xoy plane and evenly distributed on both black lines if it is not 0. (b) Band structure of the simplified ISL unit cell, in which the density of the ligaments is $1000\ \mathrm{kg/m^3}$ while m_a is 0. (c) FRF results of one simplified SYL unit cell. (d) Simplified ISL unit cell. In this simplified unit cell, L =60 mm, d_2=30 mm, d_3=26 mm, t=2 mm, h_1=10 mm. (e) Band structure of simplified ISL unit cell in which the density of the ligaments is $1000\ \mathrm{kg/m^3}$ while m_a is 0. (f) FRF results of one simplified ISL unit cell. Notable, the concentrated mass in the simulations of (e-f) is 0 and the ligaments are density-free.

151 According to the conditions of elastic Thomson scattering [58], ISL and SYL have to own translation-
152 rotation coupling. It has been demonstrated that the chirality is an effective way to achieve the motion-
153 coupling condition, thus producing the inertial amplification effect [59, 61]. However, not all chiral
154 structures have this basic property [60]. The unit cell like SYL can guarantee this property due to its
155 symmetry [60]. However, due to the lumped masses in an asymmetric lattice like ISL do not have
156 symmetry, the entire finite-period structure will be a shear movement. In the absence of external forces
157 to counteract its shear movement along the y-axis (refer to coordinate in **Fig. 4**(d)), the lumped masses
158 like ISL shown in **Fig. 4**(d) do not stably produce the motion coupling and thus provide inertial
159 amplification [60].
160 To manually avoid the shear movement along the y-axis, we allow rotation axes 1 and 2 to rotate
161 around the z-axis and move along the x-axis only. The motion of the entire system along the z-axis
162 direction is not allowed in order to avoid the interference of the z-axis modes. A harmonic uniform
163 line load along the x-axis is applied on the rotation axis 1. Two domain point probes are additional at
164 the centers of axes 1 and 2 to pick up the acceleration. The transmission is calculated as a_o/a_i.
165 In order to control variable of that avoiding the interference from the classical inertial amplification
166 form [35, 37] in the ligament domain of SYL and facilitate us to find the bandgap difference between
167 ISL and SYL, the case of non-concentrated mass at the center of the ligament is discussed first and the
168 FRFs are presented in **Fig. 4**(c) and **Fig. 4**(f).
169 Observing from **Fig. 4**(c), one can see that in SYL (**Fig. 4**(c)), the attenuation starts from the second
170 resonance peak (around 500 Hz); the attenuation curve from the second resonance peak to the 4 kHz
171 range is smooth. In terms of ISL (**Fig. 4** (f)), there are some differences compared to SYL. The first
172 one is that there is only one resonance peak before the attenuation of ISL. The attenuation range is cut
173 off at around 3500 Hz. Besides, there is an anti-resonance notch at 400 Hz, thus significantly enhancing
174 the attenuation at low frequencies.
175 In practice, the ligaments cannot be density-free. Therefore, we compared the case of ligaments with
176 homogeneous density of 1000 $\mathrm{kg/m^3}$. For SYL, when the ligament has homogeneous density, an anti-
177 resonance notch can be found at 3700 Hz. If we equate the homogeneous density to a concentrated
178 mass ($m_a = 0.2$ g), as shown in **Fig. 5**(a), both results will be similar except for the slight shift of the

second resonance peak toward the lower frequency in case of homogeneous density. It is of interest that, in ISL shown in **Fig. 5**(b), two cases have no influence on the anti-resonance notch. Besides, regardless of homogeneous density or a concentrated mass, there is only one phenomenon that a new resonance peak in 1500-2500 Hz truncate the original attenuation from 200 – 3500 Hz. Eventually, the first bandgap of ISL covers from 254 Hz to 2240 Hz (**Fig. 5**(d)), but the bandgap of SYL starts from 740 Hz (**Fig. 5**(c)) and extends beyond 4000 Hz.

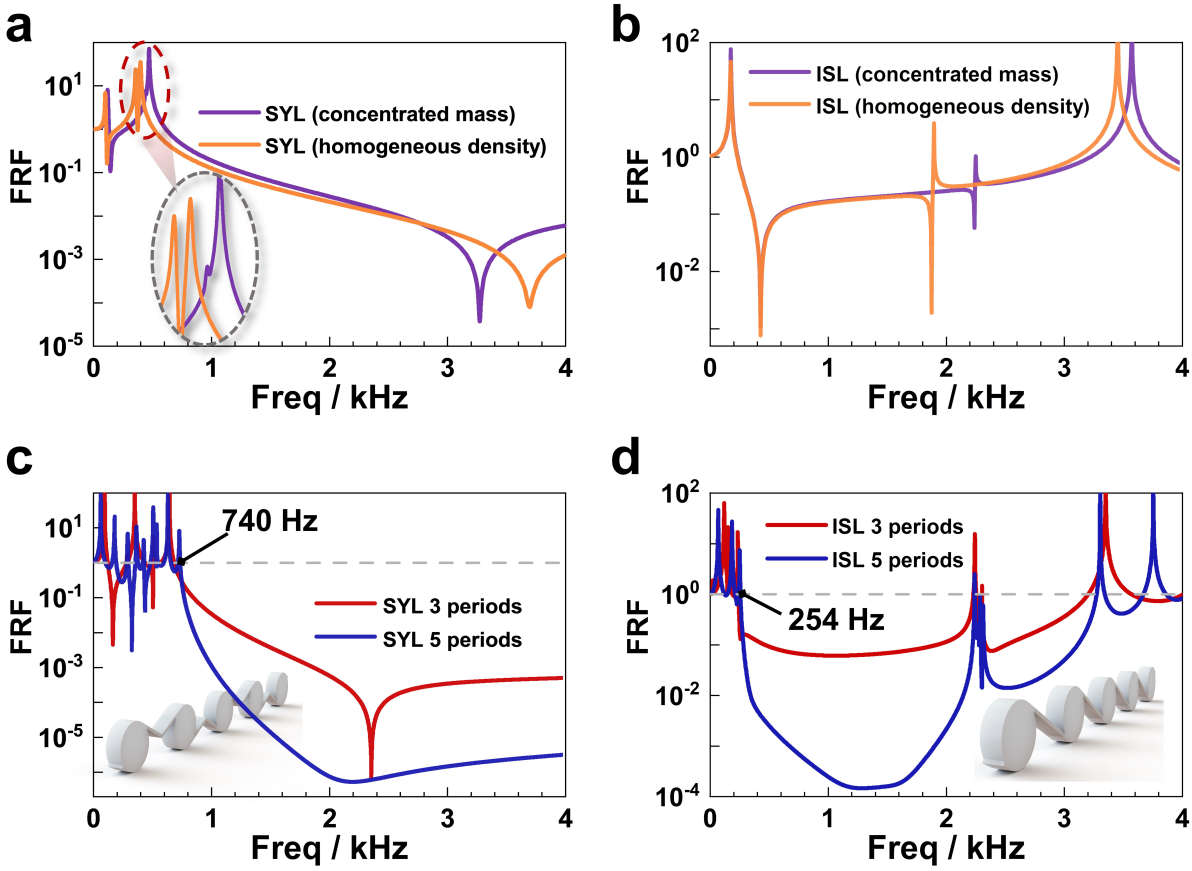

Fig. 5. (a-b) FRF results for finite structures with different boundaries. The inset in (a) reveals the resonance-peak details of the blue line. (c-d) FRF results for finite structures with different periods of simplified ISL and SYL unit cell whose ligaments are density free and have a concentrated mass of 0.2g. The insets in (c) and (d) are three-period structures of SYL and ISL, respectively. The gray lines in (c) and (d) are the reference line of attenuation.

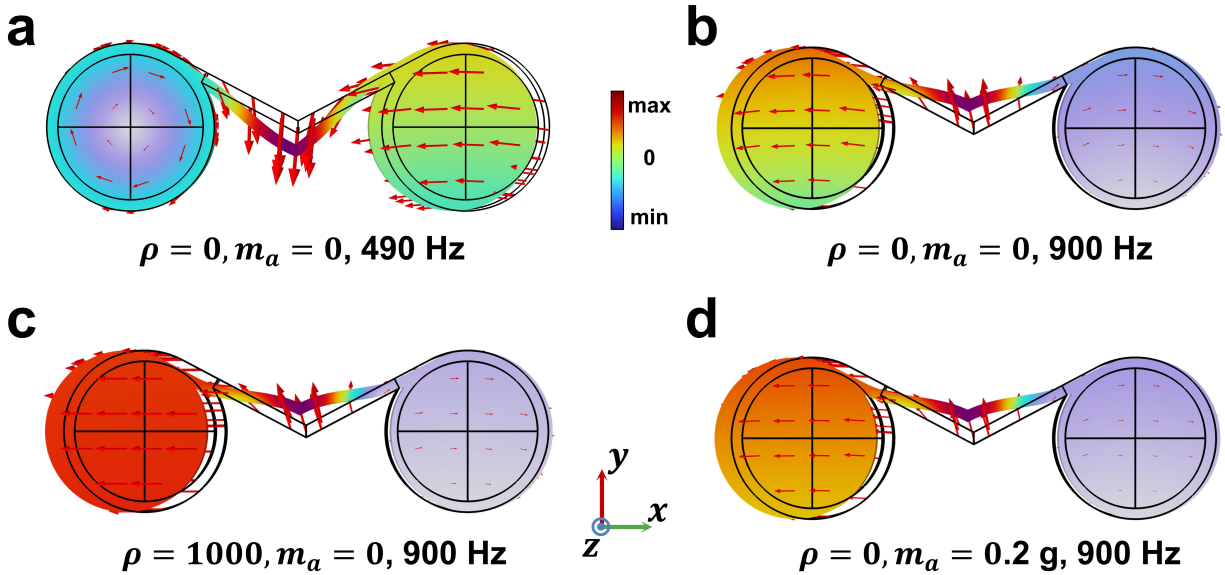

Fig. 6. The deformation contours of the simplified 1D SYL at the resonance peak and within the bandgap. (a) Deformation contour of the resonance peak when the ligament is density free and concentrated mass m_a is 0. (b) Deformation contour within the bandgap when the ligament is density free and concentrated mass m_a is 0. (b) Deformation contour within the bandgap when the density of the ligament is 1000 kg/m^3 and concentrated mass m_a is 0. (c) Deformation contour within the bandgap when the density of the ligament is 0 and concentrated mass m_a is 0.2 g.

Furthermore, we analysis the differences of the bandgap difference between ISL and SYL on deformation contours. Because ISL and SYL have different bandgap starting frequency but each one has similar starting attenuation frequency under the three conditions (i.e., density free, concentrated mass, and homogeneous), we choose the deformation contours which is the nearest to their starting attenuation, as well as the ones at 350 Hz for ISL and 900 Hz for SYL which are within the bandgap. Fig. 6 is the deformation contours of SYL and Fig. 7 is that of SYL.

In terms do the SYL, there is a folded corner, which is similar with the form of the classical inertial amplification [35, 37, 73]. The classical inertial amplification requires a concentrated mass at the folder corner, in order to provide an amplified inertia for main structures. On the one hand, the amplified inertia can decrease the resonant peaks before the bandgap, at the same time, it can induce an anti-resonance peak to enhance the attenuation of the bandgap. If the sub-structure of the inertial amplification is non-mass, the inertial amplification effect will disappear [36]. Therefore, in order to

avoid the interference from the classical inertial amplification, we compared three cases of density free, concentrated mass, and homogenous.

Fig. 6(a) shows that even though the folded corner is density-free, the resonant peak of the SYL still contains the significant motion of the folded corner in addition to that of two lumped masses, which means the resonant peak is strongly related to the folded corner. If the folded mass has a small concentrated mass, i.e., $m_a = 0.2$ g, there will be the classical inertial amplification. In this case, there will be three resonance peaks before the bandgap as shown in **Fig. 5**(a); besides, the concentrated mass will induce an anti-resonant notch in the attenuation range. Comparing Fig. 6(b) - (d), regardless the presence or absence of the classical inertial amplification, the shapes of the deformation contours within the bandgap are similar. Notably, the entire mode includes the translation and rotation of other two lumped mass, and in addition, the folded corner shows the similar transverse as the classical inertial amplification [54, 72]. In other words, the geometrical form like the classical inertial amplification sub-structure is a key factor for the second resonant peak at 490 Hz; however, it does not determine the existence of the Thomson scattering-induced bandgap but can contribute to enhancing attenuation of the bandgap since its anti-resonant notch.

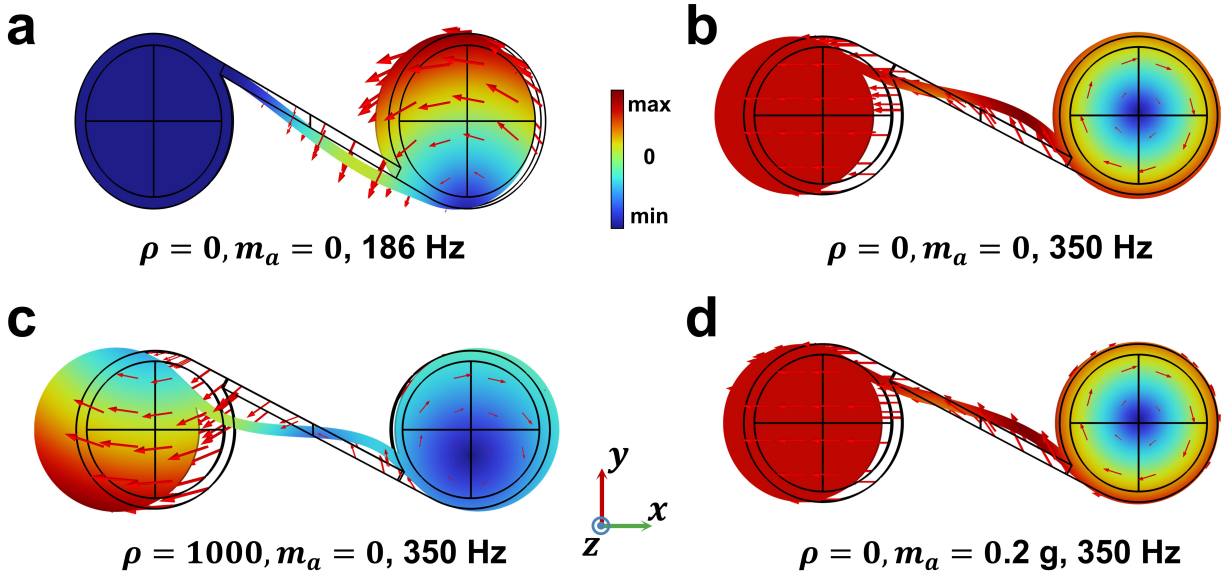

Fig. 7. The deformation contours of the simplified 1D ISL at the resonance peak and within the bandgap. (a) Deformation contour of the resonance peak when the ligament is density free and concentrated mass m_a is 0. (b) Deformation contour within the bandgap when the ligament is density free and m_a is 0. (b) Deformation contour within the bandgap when the density of the

ligament is 1000 $\mathbf{kg/m^3}$ and m_a is 0. (c) Deformation contour within the bandgap when the density of the ligament is 0 and m_a is 0.2 g.

For ISL, because the folded corner does not exist, the mode deformations become concise. Fig. 7(a) shows that the resonance peak originates from the second lumped mass and hardly involves the first concentrated mass and the significant transverse of the ligament. Even in the case of the concentrated mass or the homogenous ligament, the ligament has no obvious transverse as in SYL. Variously, when the ligament is homogenous, the two lumped masses will have rotation by deviating from their own geometric central axis. Luckly, these deformation differences have no influence on the starting frequency of the bandgap and the attenuation within the bandgap. Notably, as shown in **Fig. 5(b)**, the concentrated mass and the densely ligament will bring about an extra resonance peak at high frequencies (Refer to **Fig. 5(b)**), thus truncating this Thomson scattering-induced bandgap.

Overall, although SYL can make the realistic ligaments favorable to generate the anti-resonance peak, it cannot compensate its natural disadvantage that the resonance peaks raise the attenuation starting frequency. In particular, from the perspective in 500 Hz range, one can see that SYL has two or three resonance peaks in three cases. In the case of non-mass, the second resonant frequency of SYL is 495 Hz. However, in the ISL, there is only one resonant frequency of 190 Hz. That is because the ligaments of the SYL have a folded corner, resulting in additional degrees of freedom and thus an additional resonance peak in the FRF. In contrast, the continuous ligament of ISL makes the lack of a resonance frequency, hence the attenuation starting frequency (190 Hz) is 61.6% lower than the one of the SYL (495 Hz). With increasing periodicity, the two lattices have a difference of about 65.7% in the starting frequency, which is consistent with the prediction (the bandgap frequency of ISL is 66% lower than that of SYL) of the band structures shown in Fig. 3, and thus verified the reasonableness of the model simplification. Detailly, as shown in **Fig. 5(c) and Fig. 5(d),** the effective attenuation of the ISL starts from 254 Hz and that of the SYL starts from 740 Hz if we take FRF $= 10^0$ as reference line. This is the reason why the bandgap of ISL predicted in band structure shown in **Figs. 3** is about 66% lower than that of SYL.

4. Verification and Discussion

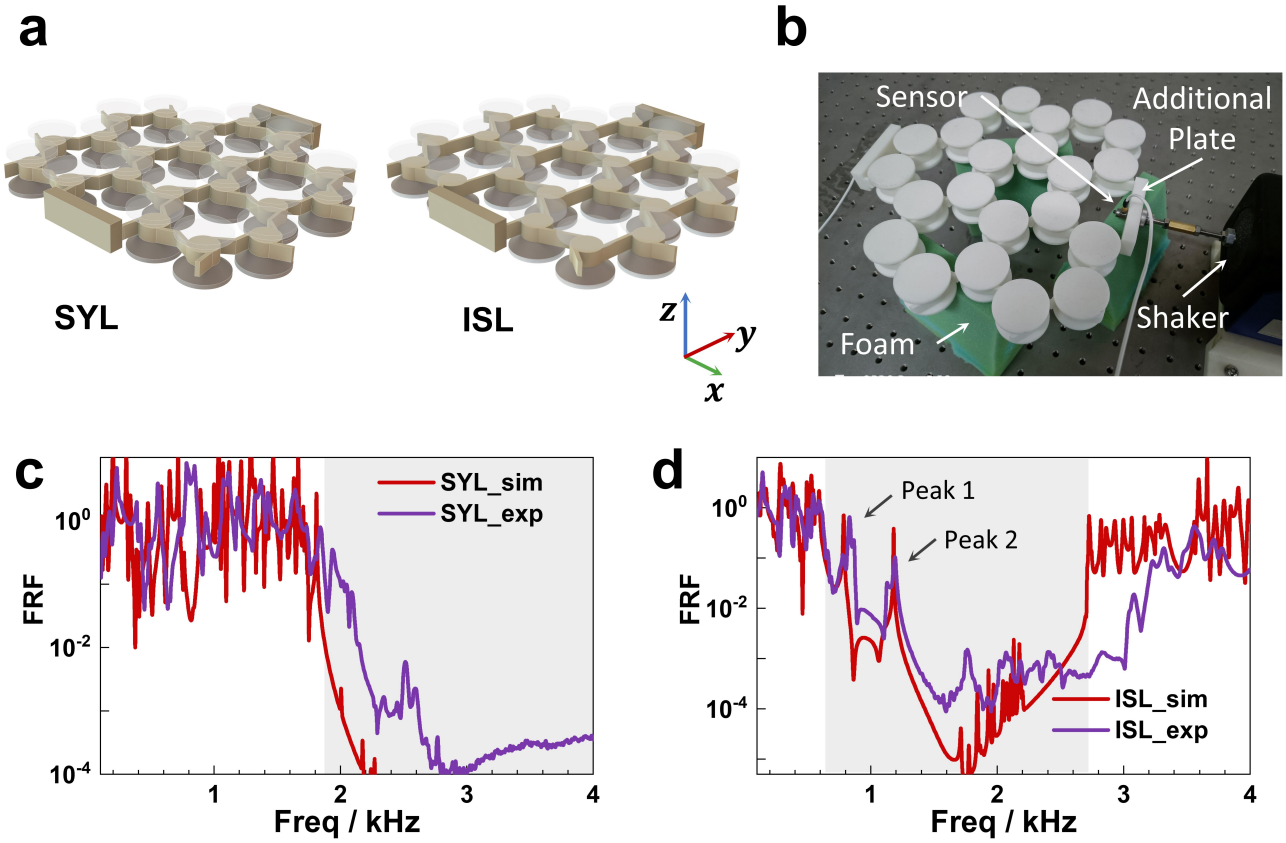

Fig. 8. (a) Schematic of the finite SYL and ISL. In order to denote the details of the ligaments, the lumped masses of the top layer are set to be transparent. (b) Experimental configuration photograph. (c) numerical and experimental results of ISL. (d) Numerical and experimental results of SYL. The shaded areas indicate the numerical bandgaps.

To validate the bandgaps predicted in the band structures, the finite-period structures of SYL (**Fig. 8**(a)) and ISL (**Fig. 8**(b)) are investigated numerically and experimentally. In simulation, two domain point probes located at the center of the additional plates are applied to acquire the input and output acceleration. The entire structure is free except the input end where a harmonic force is applied. It is notable that the out-of-plane motion of the finite period structure is free in stand of restrained as in the calculation of the band structure, because we cannot realize this ideal condition in experiment. The harmonic excitation signal sweeps from 100 Hz to 4000 Hz with the resolution of 5 Hz. As illustrated in **Fig. 8**(a), the extra additional plates are designed to connect the shaker (Modelshop K2007E01) and

sensors (PCB 353B15). The foam is used to support and level samples, as well as isolate the vibration from the optical test platform.

Fig. 8(c) and **Fig. 8**(d) show the numerical and experimental results of the ISL and SYL. For ISL, experiment and simulation denote that the bandgap appears from 600Hz to 2700Hz, while the one of the SYL starts at about 1900 Hz. Overall, the experimental measurements corroborate the numerical transmission results. Due to the manufacturing errors and the random factors in the experiment, the results shift towards high frequency compared to the simulation, such as the starting attenuation frequency in **Fig. 8**(c).

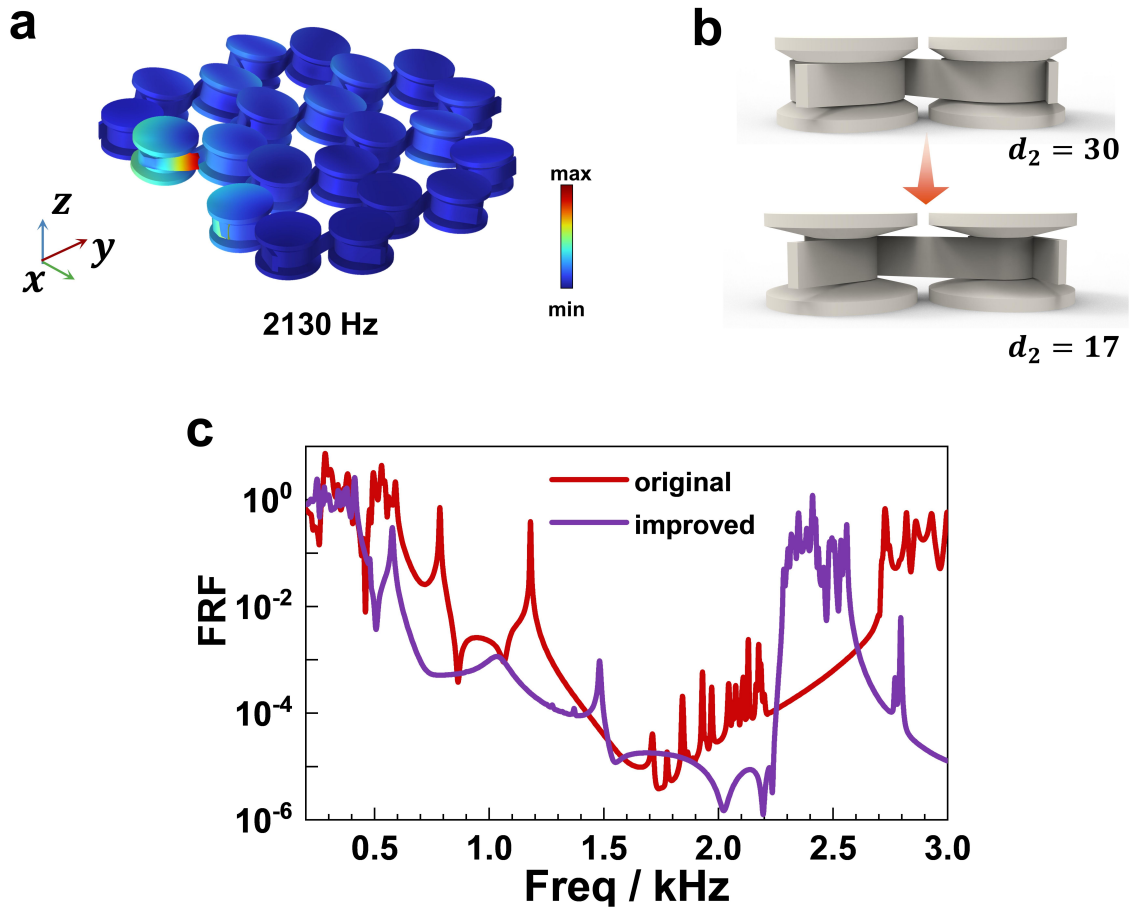

Fig. 9. (a) Deformation contour of ISL at 2130 Hz. (b) The variation in geometry of ISL to eliminate resonant peaks within 1700 Hz - 2200 Hz. (c) FRFs of original (red line) and improved (blue line) ISL

In **Fig. 8**(d), there are two obvious peaks at 785 Hz and 1180 Hz and a bunch of weak resonance peaks in 1700 Hz - 2200 Hz, thus breaking the bandgap continuity. In order to find the cause of the resonance

peaks in 1700 Hz – 2200 Hz, **Fig.** 9(c) shows the deformation contour at 2130 Hz, which reveals an out-of-plane mode. In short, the excitation in xoy plane actives the out-of-plane mode. Theoretically, the out-of-plane mode should be suppressed to be consistent with the boundaries of band-structure calculation. However, it is easy to implement in simulation but hard in experiment. In fact, the out-of-plane modes can be avoided by the structure design even if in practice we do not provide extra force on the surface of the sample to prevent its out-of-plane motion. As in the gyroscope principle, the relative angular momentum (the ratio of the rotational inertia of lumped mass to that of the circle with d_2) is small due to the small dimensional ratio of d_1 to d_3, and thus leads to the dynamic stability of the lumped mass in the xoy plane. Therefore, by increasing the difference between d_1 and d_3 (as shown in **Fig. 9**(b)), these unfavorable resonance peaks can be effectively inhibited such as illustrated in **Fig. 9**(c). This is the reason for the shape of the additional lumped mass denoted in Fig. 1(b).

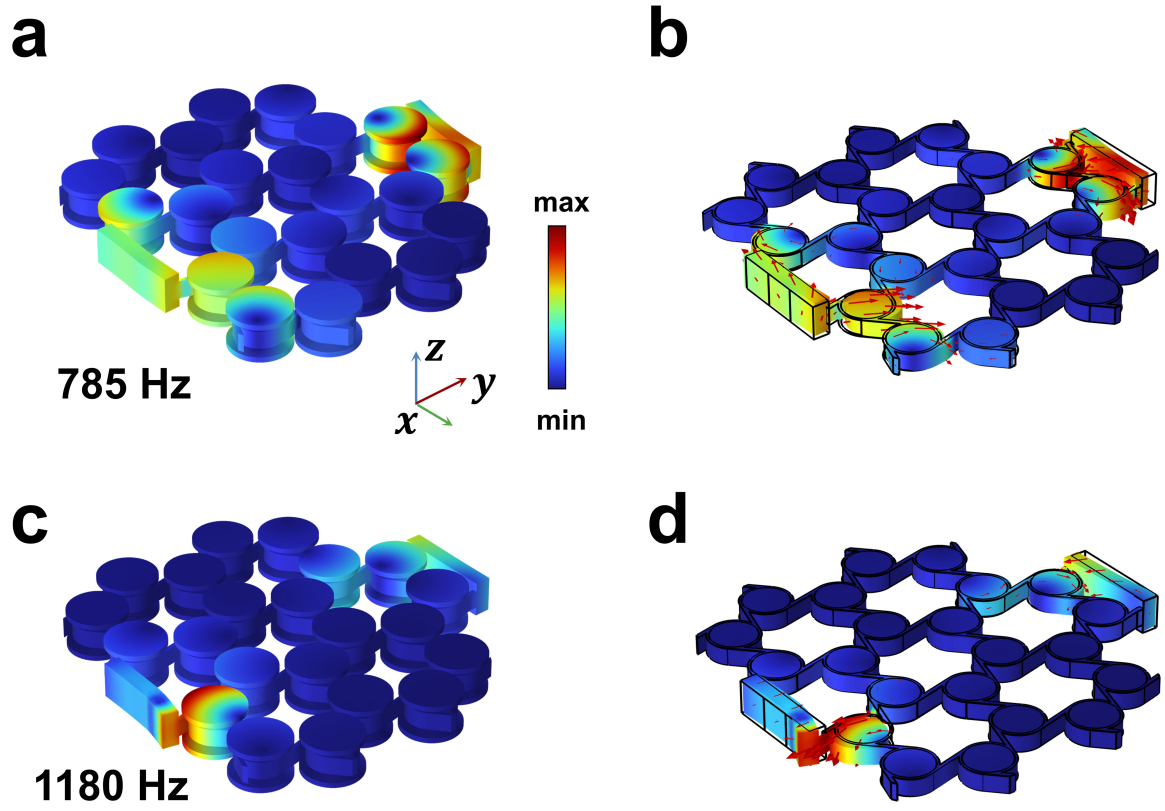

Fig. 10. Deformation contour of ISL at (a)785 Hz, (c) 1180 Hz. The ligament deformation details at (b)785 Hz, (d) 1180 Hz.

In **Fig. 8**(d), the two peaks at 785 Hz and 1180 Hz show almost no attenuation. To find the cause of these resonance peaks, the deformation contours of the entire finite structure at 785 Hz and 1180 Hz are drawn in Fig. 10(a) and Fig. 10(c); Fig. 10(b) and Fig. 10(d) show the deformations of the ligaments for more details. One can see the obvious local deformation of the additional plates and the global rotation in the lumped masses attached with the additional plates rather than the ligaments. It seems to indicate that these two peaks are strictly related to the additional plates and the lumped masses but it's not completely accurate. Therefore, we did the further discussion below.

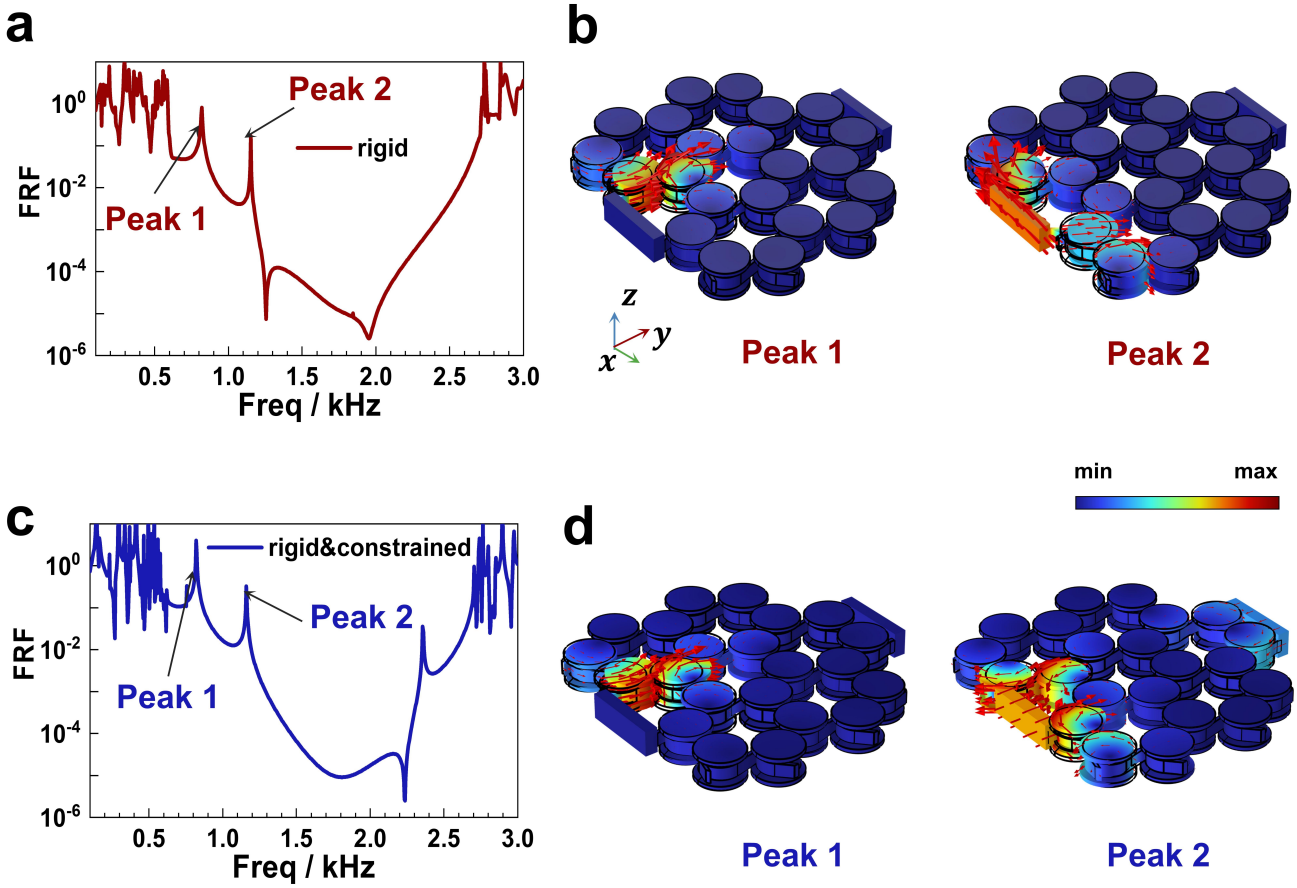

Fig. 11. (a) FRF of finite structure with rigid additional plates. (b) Deformation contour of the peak 1 and peak 2 in Fig. 11(a). (c) FRF of finite structure with rigid additional plates whose movements along x-axis and z-axis are constrained. (d) Deformation contour of the peak 1 and peak 2 in Fig. 11(c). The arrows in the deformation contours mean the surface deformation direction.

As illustrated in **Fig. 11**(a), when the additional plates are rigid to avoid the local deformation of the additional plates, the peaks still exist. In **Fig. 11**(b), the black frame is the original positions of the

period structure. Taking its original position as the reference, one can find that both deformations include the translation along the y-axis and rotation around z-axis of the lumped masses. Besides, peak 2 is not only related to the shear movement (the motion along x direction) of the additional plates, but also to the shear movement of the lumped masses. Therefore, we restrict additional plates from moving on y-axis and z-axis. Nevertheless, these peaks still exist and do not change in the frequency and value, as shown in Fig. 11(c). The arrows in **Fig. 11**(d) reveal that, these two peaks still mainly depend on the resonance modes of the lumped mass. The motion restriction for the additional plates does not change the resonance mode of the first peak, and different from the first resonance peak, the second peak involves the vibration of more lumped masses. In other words, the boundary conditions on the additional plates are not the kay factor to determine these two resonance peaks.

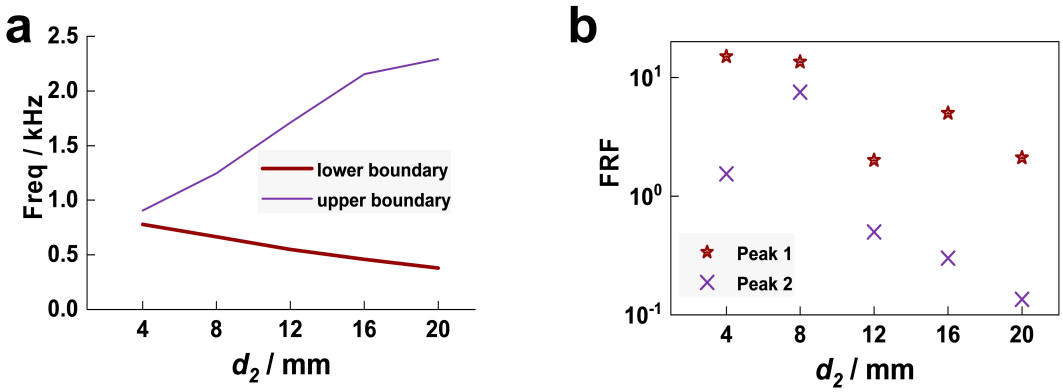

Fig. 12. Parameter discussion about geometrical dimension d_2 of ISL. (a) The influence of d_2 on the first bandgap width of ISL. (b) The influence of d_2 on the peak 1 and peak 2 of ISL. Please refer to Appendix S1 to find the variation principle of d_2.

It is worth noting that the resonance modes corresponding to these two peaks are asymmetric in the xoy plane. This is due to the fact that ISL is asymmetry, which leads to unequal contributions of the input wave to the connected ligaments on both sides. It is to be expected that the asymmetry will get smaller and smaller with the decrease of d_2. However, as illustrated by Fig. 12, when $d_2 = 4$ mm, the width of the bandgap drops rapidly to almost close. Nevertheless, these two peaks are still greater than 10^0. Briefly, it is undesirable to completely eliminate this asymmetry, because the asymmetry is the critical condition to produce the motion coupling of the lumped mass and motion coupling is fundamental condition for Thomson scattering-induced bandgap. If decreasing d_2 continuously, the

asymmetry will gradually go forward to symmetry, and then ISL will evolve to BRL. Consequently, the Thomson scattering-induced bandgap will disappear.

Generally, the equivalent stiffness and density of the system are two underlying factors on the resonance peaks. Within all geometrical parameters, increasing lattice constant can modify the length of the ligaments and thus control equivalent stiffness; varying the density of the lumped masses can manipulate the equivalent density of the system independently. In order to control a single variable, the lattice constant changes or the density changes while all other parameters remain constant (Please refer to Appendix S1 to find the variation principle of the lattice constant). Fig. **13** shows the results of the parameter discussion about density and lattice constant. From **Fig. 13(a)**, one can see that the suppression for these two resonance peaks isn't absolutely better with the increase of the density. For peak 1, regardless the density variation, it still exceeds $\mathbf{10^0}$; but for peak 2, there seems to be a great value when density is 3000 to 5000 $\mathbf{kg/m^3}$. Fortunately, **Fig. 13(b)** reveals that both peaks will show attenuation when the lattice constant is larger than 100 mm. In short, the combination adjustment for equivalent stiffness and equivalent density can indeed be a strategy to suppress these two unfavorable resonance peaks. Therefore, as denoted by the case in **Fig. 14**, through increasing the lattice constant and the asymmetry of the ISL unit cell for modifying stiffness, and increasing the dimension of lumped masses for adjusting equivalent density of the unit cell, we can weaken the performance of these two peaks in the FRF. (Please refer to **Appendix S2** to find the geometrical details).

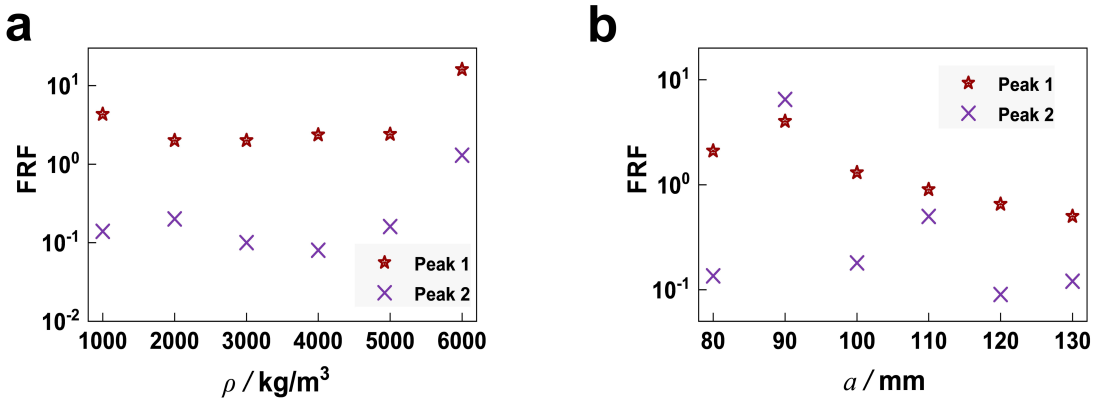

Fig. 13. Parameter discussion about the influence of (a) the lattice constant variation and (b) the density of the lumped masses on peak 1 and peak 2. All other geometries keep constant when the

lattice constant changes. Please refer to Appendix S1 to find the variation principle of the lattice constant.

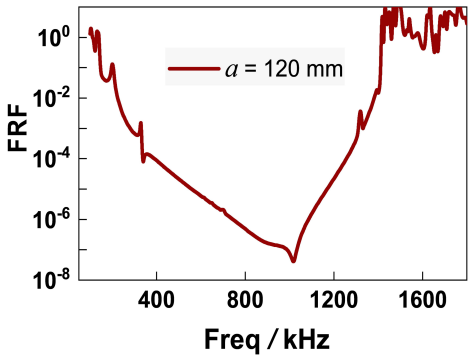

Fig. 14. FRF of finite structure with lattice constant $a = 120$ mm. In numerical calculation, the additional plates have an elastic modulus of 1.6e13 Pa and "density free" indicates that the density of the additional plates is 0 while the one of the rest components in finite structure is 1000 kg/m^3. Compared to the ISL mentioned in Fig. 1, the altered dimensions of the unit cell can be found in table 1 attached to Appendix S2. Other conditions are keeping constant.

5. Conclusion

In summary, this study has reported an isotactic chiral phononic crystal with a Thomson scattering-induced bandgap for a low-frequency and broad bandgap. The band structures of the classical Bragg scattering, sydiotactic, and isotactic lattices have been numerically calculated and compared together to elucidate the novelty of the isotactic chiral phononic crystals. The band structures and FRFs of simplified one-dimensional ISL and SYL have been compared to find the cause of the bandgap difference in ISL and SYL. Then the finite period structures have been designed, manufactured, and tested for the transmission, to verify the bandgap prediction in the band structure. Based on above study, the following conclusion can be drawn.

Distinct from previous studies in which the sydiotactic phononic crystals are considered as a more superior way to realize low-frequency and broad bandgaps than isotactic phononic crystals [57, 61, 74, 75], we have verified that although both ISL and SYL have the motion coupling which is one of the way to achieve the inertial amplification [60], the lack of the mirror symmetry makes the ISL having one less degree of freedom than SYL and hence there is less a resonant peak than SYL. As a result,

the bandgap starting frequency of ISL is lower by 66% than that of SYL. In addition, the relative width of the bandgap of up to 129% can be guaranteed. This research has illustrated that the condition of having alternating arrangement orientations between neighboring atoms is not indispensable for bandgap formation. These variances between the SYL and ISL do not depend on altering the lattice constant, equivalent stiffness, and static equivalent density of the system. The consequent radically unusual behaviors may make this design strategy attractive in all the fields where vibrations play a crucial role, such as for instance civil, aerospace and mechanical engineering.

Appendix S1

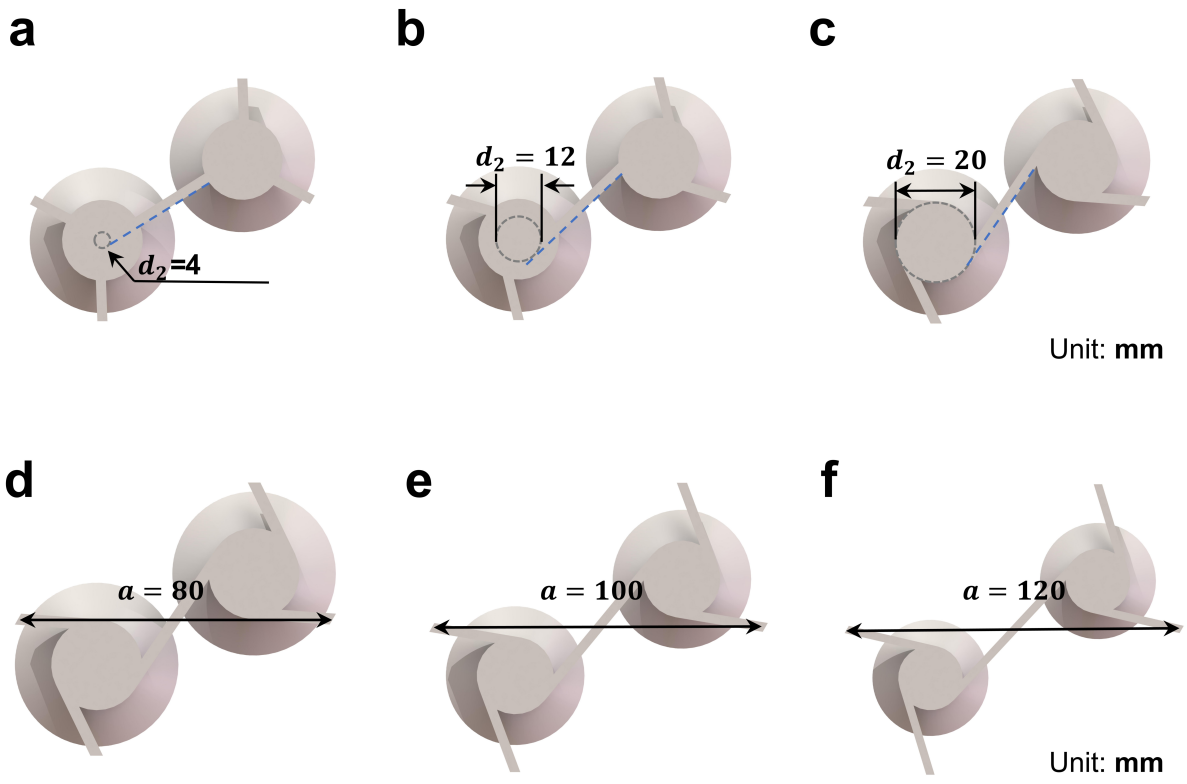

Fig. S1. The variation principle of (a-c) the diameter d_2 and (d-f) the lattice constant.

Appendix S2

Table 1. Dimensions of ISL in Fig. 13

Parameter	a	d_1	d_2	d_3
Dimension	120	50	30	25

Acknowledgment

This work was financially supported by the National Natural Science Foundation of China (No. 12002258), and the China Postdoctoral Science Foundation (No. 2022M712540). Wei Ding is grateful to the support of China Scholarship Council (Grant No. 202206280170). Wei Ding thanks Huan Lu (Xi'an Jiaotong University) for his help in the analysis of the study problem.

References

[1] Oudich M, Gerard NJRK, Deng Y, Jing Y. Tailoring Structure‐Borne Sound through Bandgap Engineering in Phononic Crystals and Metamaterials: A Comprehensive Review. Adv Funct Mater. 2022;33:2206309.

[2] Brule S, Javelaud EH, Enoch S, Guenneau S. Experiments on seismic metamaterials: molding surface waves. Phys Rev Lett. 2014;112(13):133901.

[3] Nomura M, Laude V, Maldovan M. Phononic crystals at various frequencies. APL Materials. 2022;10(5):050401.

[4] Maldovan M. Narrow Low-Frequency Spectrum and Heat Management by Thermocrystals. Phys Rev Lett. 2013;110(2):025902.

[5] Wang J-Q, Zhang Z-D, Yu S-Y, Ge H, Liu K-F, Wu T, et al. Extended topological valley-locked surface acoustic waves. Nat Commun. 2022;13(1):1324.

[6] Zheng S, Man X, Kong Z-L, Lin Z-K, Duan G, Chen N, et al. Observation of fractal higher-order topological states in acoustic metamaterials. Science Bulletin. 2022;67(20):2069-75.

[7] Kushwaha MS, Halevi P, Dobrzynski L, Djafari-Rouhani B. Acoustic band structure of periodic elastic composites. Phys Rev Lett. 1993;71(13):2022-5.

[8] Liu Z, Zhang X, Mao Y, Zhu YY, Yang Z, Chan CT, et al. Locally Resonant Sonic Materials. Science. 2000;289(5485):1734-6.

[9] Celli P, Yousefzadeh B, Daraio C, Gonella S. Bandgap widening by disorder in rainbow metamaterials. Appl Phys Lett. 2019;114(9):091903.

[10] De Ponti JM, Iorio L, Riva E, Ardito R, Braghin F, Corigliano A. Selective Mode Conversion and Rainbow Trapping via Graded Elastic Waveguides. Phys Rev Appl. 2021;16(3):034028.

[11] Meng H, Chronopoulos D, Fabro AT, Elmadih W, Maskery I. Rainbow metamaterials for broadband multi-frequency vibration attenuation: Numerical analysis and experimental validation. J Sound Vib. 2020;465:115005.

[12] Baravelli E, Ruzzene M. Internally resonating lattices for bandgap generation and low-frequency vibration control. J Sound Vib. 2013;332(25):6562-79.

[13] De Ponti JM, Colombi A, Ardito R, Braghin F, Corigliano A, Craster RV. Graded elastic metasurface for enhanced energy harvesting. New J Phys. 2020;22(1):013013.

[14] Li C, Jiang T, He Q, Peng Z. Stiffness-mass-coding metamaterial with broadband tunability for low-frequency vibration isolation. J Sound Vib. 2020;489:115685.

[15] Hu G, C. M. Austin A, Sorokin V, Tang L. Metamaterial beam with graded local resonators for broadband vibration suppression. Mech Syst Sig Process. 2021;146:106982.
[16] Liu L, Hussein MI. Wave Motion in Periodic Flexural Beams and Characterization of the Transition Between Bragg Scattering and Local Resonance. J Appl Mech. 2012;79(1):011003.
[17] D'Alessandro L, Belloni E, Ardito R, Corigliano A, Braghin F. Modeling and experimental verification of an ultra-wide bandgap in 3D phononic crystal. Appl Phys Lett. 2016;109(22):221907.
[18] Matlack KH, Bauhofer A, Krödel S, Palermo A, Daraio C. Composite 3D-printed metastructures for low-frequency and broadband vibration absorption. Proc Natl Acad Sci USA. 2016;113(30):8386-90.
[19] Tian X, Chen W, Gao R, Liu S. Merging Bragg and Local Resonance Bandgaps in Perforated Elastic Metamaterials with Embedded Spiral Holes. J Sound Vib. 2021;500:116036.
[20] Park HW, Seung HM, Kim M, Choi W, Oh JH. Continuum Flexural Metamaterial for Broadband Low-Frequency Band Gap. Phys Rev Appl. 2021;15(2):024008.
[21] Park S, Jeon W. Ultra-wide low-frequency band gap in a tapered phononic beam. J Sound Vib. 2021;499:115977.
[22] Fang X, Wen J, Bonello B, Yin J, Yu D. Ultra-low and ultra-broad-band nonlinear acoustic metamaterials. Nat Commun. 2017;8(1):1288.
[23] Zhou J, Dou L, Wang K, Xu D, Ouyang H. A nonlinear resonator with inertial amplification for very low-frequency flexural wave attenuations in beams. Nonlinear Dyn. 2019;96(1):647-65.
[24] Yang H, Xu J, Xiong Z, Lu X, Zhang R-Y, Li H, et al. Optically Reconfigurable Spin-Valley Hall Effect of Light in Coupled Nonlinear Ring Resonator Lattice. Phys Rev Lett. 2021;127(4):043904.
[25] Yu J, Park S, Hwang I, Kim D, Demmerle F, Boehm G, et al. Electrically tunable nonlinear polaritonic metasurface. Nature Photonics. 2022;16(1):72-8.
[26] Cai C, Zhou J, Wang K, Pan H, Tan D, Xu D, et al. Flexural wave attenuation by metamaterial beam with compliant quasi-zero-stiffness resonators. Mech Syst Sig Process. 2022;174:109119.
[27] Zhang Q, Guo D, Hu G. Tailored Mechanical Metamaterials with Programmable Quasi‐Zero‐Stiffness Features for Full‐Band Vibration Isolation. Adv Funct Mater. 2021;31(33):2101428.
[28] Wang K, Zhou J, Ouyang H, Chang Y, Xu D. A dual quasi-zero-stiffness sliding-mode triboelectric nanogenerator for harvesting ultralow-low frequency vibration energy. Mech Syst Sig Process. 2021;151:107368.
[29] Jia Z, Chen Y, Yang H, Wang L. Designing Phononic Crystals with Wide and Robust Band Gaps. Phys Rev Appl. 2018;9(4):044021.
[30] Lucklum F, Vellekoop MJ. Bandgap engineering of three-dimensional phononic crystals in a simple cubic lattice. Appl Phys Lett. 2018;113(20):201902.
[31] Salari-Sharif L, Haghpanah B, Guell Izard A, Tootkaboni M, Valdevit L. Negative-Stiffness Inclusions as a Platform for Real-Time Tunable Phononic Metamaterials. Phys Rev Appl. 2019;11(2):024061.
[32] Fei X, Jin L, Zhang X, Li X, Lu M. Three-dimensional anti-chiral auxetic metamaterial with tunable phononic bandgap. Appl Phys Lett. 2020;116(2):021902.
[33] Gerard NJRK, Oudich M, Xu Z, Yao D, Cui H, Naify CJ, et al. Three-Dimensional Trampolinelike Behavior in an Ultralight Elastic Metamaterial. Phys Rev Appl. 2021;16(2):024015.

[34] Iglesias Martínez JA, Moughames J, Ulliac G, Kadic M, Laude V. Three-dimensional phononic crystal with ultra-wide bandgap at megahertz frequencies. Appl Phys Lett. 2021;118(6):063507.
[35] Yilmaz C, Hulbert GM, Kikuchi N. Phononic band gaps induced by inertial amplification in periodic media. Phys Rev B. 2007;76(5):054309.
[36] Yilmaz C, Kikuchi N. Analysis and design of passive low-pass filter-type vibration isolators considering stiffness and mass limitations. J Sound Vib. 2006;293(1-2):171-95.
[37] Yilmaz C, Hulbert GM. Theory of phononic gaps induced by inertial amplification in finite structures. Phys Lett A. 2010;374(34):3576-84.
[38] Acar G, Yilmaz C. Experimental and numerical evidence for the existence of wide and deep phononic gaps induced by inertial amplification in two-dimensional solid structures. J Sound Vib. 2013;332(24):6389-404.
[39] Xiao Y, Wen J, Yu D, Wen X. Flexural wave propagation in beams with periodically attached vibration absorbers: Band-gap behavior and band formation mechanisms. J Sound Vib. 2013;332(4):867-93.
[40] Taniker S, Yilmaz C. Design, analysis and experimental investigation of three-dimensional structures with inertial amplification induced vibration stop bands. Int J Solids Struct. 2015;72:88-97.
[41] Sun Y, Zheng H, Lee HP. Beam-type metastructure with X-shape inertial amplification mechanisms for vibration suppression. Thin Wall Struct. 2023;189:110893.
[42] Li J, Yang P, Li S. Multiple band gaps for efficient wave attenuation by inertial amplification in periodic functionally graded beams. Compos Struct. 2021;271:114130.
[43] Zeng Y, Cao L, Wan S, Guo T, Wang Y-F, Du Q-J, et al. Seismic metamaterials: Generating low-frequency bandgaps induced by inertial amplification. Intl J Mech Sci. 2022;221:107224.
[44] Frandsen NMM, Bilal OR, Jensen JS, Hussein MI. Inertial amplification of continuous structures: Large band gaps from small masses. J Appl Phys. 2016;119(12):124902.
[45] Xi C, Dou L, Mi Y, Zheng H. Inertial amplification induced band gaps in corrugated-core sandwich panels. Compos Struct. 2021;267:113918.
[46] Zeng Y, Cao L, Wan S, Guo T, An S, Wang Y-F, et al. Inertially amplified seismic metamaterial with an ultra-low-frequency bandgap. Appl Phys Lett. 2022;121(8):081701.
[47] Li L, Wang Q, Liu H, Li L, Yang Q, Zhu C. Seismic metamaterials based on coupling mechanism of inertial amplification and local resonance. Physica Scripta. 2023;98(4):045024.
[48] Zhao C, Zhang K, Zhao P, Hong F, Deng Z. Bandgap merging and backward wave propagation in inertial amplification metamaterials. Intl J Mech Sci. 2023;250:108319.
[49] Mu D, Wang K, Shu H, Lu J. Metamaterial beams with graded two-stage inertial amplification and elastic foundation. Intl J Mech Sci. 2022;236:107761.
[50] Mazzotti M, Foehr A, Bilal OR, Bergamini A, Bosia F, Daraio C, et al. Bio-inspired non self-similar hierarchical elastic metamaterials. Intl J Mech Sci. 2023;241:107915.
[51] Cai C, Zhou J, Wu L, Wang K, Xu D, Ouyang H. Design and numerical validation of quasi-zero-stiffness metamaterials for very low-frequency band gaps. Compos Struct. 2020;236:111862.
[52] Li J, Yang P, Li S. Phononic band gaps by inertial amplification mechanisms in periodic composite sandwich beam with lattice truss cores. Compos Struct. 2020;231:11458.
[53] Muhammad S, Wang S, Li F, Zhang C. Bandgap enhancement of periodic nonuniform metamaterial beams with inertial amplification mechanisms. J Vib Control. 2020;26(15-16):1309-18.

[54] Yuksel O, Yilmaz C. Realization of an ultrawide stop band in a 2-D elastic metamaterial with topologically optimized inertial amplification mechanisms. Int J Solids Struct. 2020;203:138-50.
[55] Banerjee A, Adhikari S, Hussein MI. Inertial amplification band-gap generation by coupling a levered mass with a locally resonant mass. Intl J Mech Sci. 2021;207:106630.
[56] Orta AH, Yilmaz C. Inertial amplification induced phononic band gaps generated by a compliant axial to rotary motion conversion mechanism. J Sound Vib. 2019;439:329-43.
[57] Bergamini A, Miniaci M, Delpero T, Tallarico D, Van Damme B, Hannema G, et al. Tacticity in chiral phononic crystals. Nat Commun. 2019;10(1):4525.
[58] Ding W, Chen T, Chen C, Chronopoulos D, Assouar B, Zhu J. Experimental Observation and Description of Bandgaps Opening in Chiral Phononic Crystals by Analogy with Thomson scattering. Preprint doi:1048550/arxiv220704282. 2022.
[59] Park J, Lee D, Jang Y, Lee A, Rho J. Chiral trabeated metabeam for low-frequency multimode wave mitigation via dual-bandgap mechanism. Commun Phys. 2022;5(1):194.
[60] Ding W, Chen T, Chen C, Chronopoulos D, Zhu J, Assouar B. Thomson scattering-induced bandgap in planar chiral phononic crystals. Mech Syst Sig Process. 2023;186:109922.
[61] Zhao P, Zhang K, Hong F, Deng Z. Tacticity-based one-dimensional chiral equilateral lattice for tailored wave propagation and design of elastic wave logic gate. J Sound Vib. 2022;521:116671.
[62] Zhao P, Zhang K, Qi L, Deng Z. 3D chiral mechanical metamaterial for tailored band gap and manipulation of vibration isolation. Mech Syst Sig Process. 2022;180:109430.
[63] Barys M, Zalewski R. Analysis of inertial amplification mechanism with smart spring-damper for attenuation of beam vibrations. Matec Web of Conferences. 2018;157:03002.
[64] Paukkeri R, Väänänen T, Lehtinen A. Microstructural analysis of polypropylenes produced with heterogeneous Ziegler-Natta catalysts. Polymer. 1993;34(12):2488-94.
[65] Alamo RG, Kim M-H, Galante MJ, Isasi JR, Mandelkern L. Structural and kinetic factors governing the formation of the γ polymorph of isotactic polypropylene. Macromolecules. 1999;32(12):4050-64.
[66] Ding W, Chen T, Chen C, Chronopoulos D, Zhu J. A three-dimensional twisted phononic crystal with omnidirectional bandgap based on inertial amplification by utilizing translation-rotation coupling. J Sound Vib. 2022;541:117307.
[67] Li H, Hu Y, Huang H, Chen J, Zhao M, Li B. Broadband low-frequency vibration attenuation in 3D printed composite meta-lattice sandwich structures. Compos B Eng. 2021;215:108772.
[68] Bilal OR, Ballagi D, Daraio C. Architected Lattices for Simultaneous Broadband Attenuation of Airborne Sound and Mechanical Vibrations in All Directions. Phys Rev Appl. 2018;10(5):054060.
[69] Phani AS, Woodhouse J, Fleck NA. Wave propagation in two-dimensional periodic lattices. J Acous Soc Am. 2006;119(4):1995-2005.
[70] Delpero T, Hannema G, Damme BV, Schoenwald S, Zemp A, Bergamini A. Inertia Amplification in Phononic Crystals for Low Frequency Band Gaps. VIII ECCOMAS Thematic Conference on Smart Structures and Materials SMART 20172017. p. 1657-68.
[71] Lu H, Wang X, Chen T. Design and quasi-static responses of a hierarchical negative Poisson's ratio structure with three plateau stages and three-step deformation. Compos Struct. 2022;291:11591.
[72] Taniker S, Yilmaz C. Generating ultra wide vibration stop bands by a novel inertial amplification mechanism topology with flexure hinges. Int J Solids Struct. 2017;106-107:129-38.

[73] Yuksel O, Yilmaz C. Shape optimization of phononic band gap structures incorporating inertial amplification mechanisms. J Sound Vib. 2015;355:232-45.
[74] Ding W, Chen T, He Y, Chen C, Huang W, Jiang Z, et al. 3D syndiotactic elastic metastructure with single-phase material. Phys Lett A. 2020;384(35):126892.
[75] Zhou Y, Ye L, Chen Y. Investigation of novel 3D-printed diatomic and local resonant metamaterials with impact mitigation capacity. Intl J Mech Sci. 2021;206:106632.